Preliminary study of saturated water (R-718) film boiling in a grooved plate evaporator

Florine Giraud, Romain Collignon, Joris Marek, Benoît Stutz

To cite this version:

Florine Giraud, Romain Collignon, Joris Marek, Benoît Stutz. Preliminary study of saturated water (R-718) film boiling in a grooved plate evaporator. International Congrès of Refrigeration, Aug 2023, Paris, France. 10.18462/iir.10.18462/iir.icr.2023.0621 . hal-04620078

HAL Id: hal-04620078
https://hal.science/hal-04620078v1

Submitted on 21 Jun 2024

DOI: 10.18462/iir. 10.18462/iir.icr.2023.0621

Preliminary study of saturated water (R-718) film boiling in a grooved plate evaporator

Florine GIRAUD[*(a)], Romain COLLIGNON[(a)], Joris MAREK[(a)], Benoît STUTZ[(a)]

[(a)] LOCIE, Université Savoie Mont Blanc, CNRS UMR5271, Savoie Technolac, 73376 Le Bourget Du Lac, France

*Corresponding author: florine.giraud@univ-smb.fr

ABSTRACT

Since it is a natural and ecological fluid with high latent heat of vaporization and high heat capacity, water (R-718) could be a good candidate to develop durable solution and replace non-environmentally friendly fluids currently used as refrigerant. However, due to several drawbacks, like the high wall superheat required to onset the boiling in these systems, evaporators currently used in water systems are mainly of falling film type. In order to allow compact design of these latter, a grooved plate falling film heat exchanger has been tested. To take advantage of boiling events observed and allow a deeper understanding of this phenomenon, a preliminary study is conducted. Boiling events observed in a saturated liquid film and in working conditions representative to those obtained in water refrigeration systems are identified and characterized using high speed imaging. The bubbles flow velocities are estimated and phenomena observed discussed.

Keywords: film boiling, water, falling-film evaporator, bubbles velocity, compact component

1. INTRODUCTION

Using water as refrigerant means using a non-toxic and environmentally-friendly fluid with interesting thermophysical properties to efficiently transfer heat. It is thus a fluid which can play a significant role in the reduction of greenhouse gases and deserves to be promoted as replacement fluid to conventional working fluid. But using water (R-718) means also various drawbacks such as high volumetric flow rate, limitation to above-0 °C applications, technical challenges to deal with near vacuum conditions, etc. Especially, boiling phenomenon are different from those observed at higher pressure. A direct result of this is usual compact heat-exchanger cannot be used. Indeed, several studies highlight the difficulty to onset the boiling partly explaining the low performances of exchangers in these systems compared with performances obtained at higher pressure (Giraud *et al.*,2015). Falling liquid films are generally preferred as heat and mass exchangers since they show significantly better performance than low-pressure boiling exchanger even at low superheat. However, they are limited by the thickness of the liquid films required to wet the walls and the low thermal conductivity of the fluids used. Their performances are thus still far from performances that could be reached if boiling is used as the major phenomenon to transfer heat and their design is not compact. Falling film boiling, on the other hand, may outperform pool-boiling heat transfer (Bock and al., 2019). Falling film boiling evaporators can thus allow to guarantee performances of falling film heat exchanger at low superheat while leading to efficient heat transfer at higher wall superheat. However, research conducted on this topic do not allow to fully understand falling film boiling. Despite the similar decrease of falling film boiling heat transfer coefficient with the saturation pressure (Bock et al., 2019), film boiling and pool-boiling are fundamentally different (Cerza and Sernas, 1985). In particular, studies highlight that the bubble growth rate is larger in film boiling than in pool-boiling. In addition, bubble sizes may be larger than the ambient film thickness. These differences added to the particularity of boiling at low pressure make observed phenomena really difficult to predict. The aim of this study is thus to go deeper into the understanding of water falling film boiling by studying phenomena observed near vacuum pressure, at conditions representatives to conditions obtained in the evaporator of a water chiller. The results presented here are preliminary results based on a wide experimental campaign. The experimental set-up is first introduced. Then, bubble velocities and area estimated through a home-made program are introduced before analysing phenomena observed for one specific condition.

2. EXPERIMENTAL SET-UP AND PROCEDURE

2.1. Experimental apparatus

The experimental set-up used to conduct the present study is introduced in Fig. 1. It is mainly constituted of a low-pressure tank (LP vessel in Fig.1) inside which the evaporator (Evap in Fig. 1) and a helicoidal condenser (Cd in Fig. 1) are inserted. The low-pressure tank is a stainless-steel cylinder 650 mm long with an external diameter of 650 mm. This cylinder is laid horizontally and two circular lateral doors made of aluminium close the volume thus created. These two doors are equipped with viewports of diameter 250 mm in order to allow visualization of phenomena occurring inside the tank. Openings with ISO-KF type plugs allow connecting the tank to hydraulic circuits and removing the air from the tank.

The studied evaporator is a falling film grooved plate evaporator of 100 mm long and 320 mm high made of aluminium. The external surface on which the working fluid flows is made of 16 grooves of 4 mm long and 1 mm depth. At the top of this latter, 70 mm of the 320 mm are used to homogeneously distribute the fluid through a home-made distributor. The secondary fluid ("heating fluid" in Fig. 2) flows in a counter-current manner inside rectangular internal channels of 4 mm width and 2 mm thick.

In this experimental set-up, the working fluid (degassed water named "Falling film" in Fig. 2) flows inside the distributor and then falls inside the 16 grooves. As it falls, a part of the fluid is vaporized (boiling and evaporation) and condensed on the external surface of the helical condenser. The remaining fluid (not vaporized) is collected at the end of the evaporator and flows to a water tank where condensed water coming from the condenser is also stored.

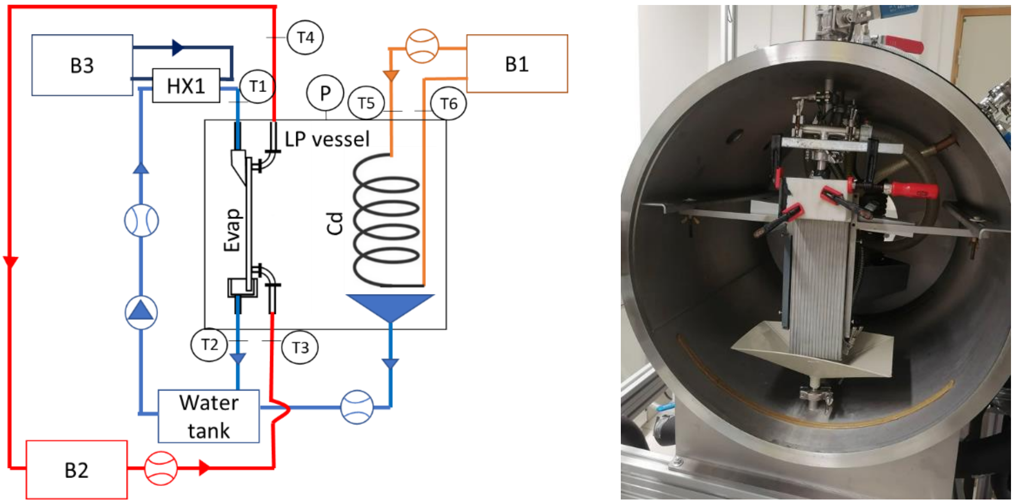

Figure 1: a) Schematic view of the experimental test set-up; b) picture of the grooved plate evaporator inside the low-pressure vessel

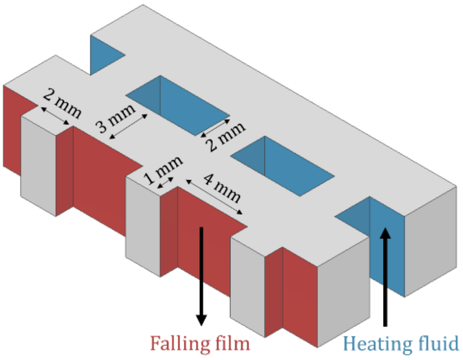

Figure 2: Schematic cross-sectional view of the grooved plate evaporator (Collignon and Stutz, 2023)

Four thermostatic baths are used to control respectively the temperature of the secondary fluid flowing inside the evaporator (B2 in Fig. 1), the temperature of the secondary fluid flowing inside the condenser (B1 in Fig. 1), the temperature of the working fluid before entering the tank (B3 in Fig. 2) and the temperature of the water tank (not represented in Fig. 1). The pressure inside the tank is controlled by the temperature set at the condenser (thermostatic bath B1) so that the pressure set is close to the one given by Eq. (1).

$$P_{tank} \approx P_{sat}(T_{cd}) \quad \text{Eq. (1)}$$

With P_{tank} the pressure measured inside the low-pressure vessel, P_{sat} (T_{cd}) the saturation pressure of the water at the condenser temperature.

P_{tank} is measured by a pressure device located at the upper part of the vessel. The associated uncertainty is +/- 0.2 % of the measured value. Six PT100 probes allow measuring the temperature of each fluid at the inlet and outlet of each component before entering the tank. The estimated uncertainties of the six PT 100 are +/- 0.1 °C. Coriolis mass-flow meters with an uncertainty of 0.1 % of the measured value are used to measure the mass flow in each hydraulic circuit as well as the amount of water collected at the outlet of the condenser.

2.2. Experimental domain and data reduction

The experimental domain covered during this study is shown in Table 1. The maximal theoretical superheat ($\Delta T_{th,max}$) is calculated as the temperature difference between the saturation temperature of the water at P_{tank} and the inlet secondary fluid temperature at the evaporator.

Table 1. Experimental domain covered

Working pressure (P_{tank} - kPa)	Saturation temperature (°C)	Maximal theoretical superheat $\Delta T_{th,max}$ (K)
1 - 2.4 kPa	7 – 20 °C	1 – 10 K

The secondary fluid mass flow rate at the condenser is set at 0.28 kg/s, and the secondary fluid mass flow rate at the evaporator at 0.025 kg/s. In order to be sure to completely wet the grooves before starting the experiments, the working fluid mass flow rate is first set at the highest mass flow rate reachable within the experimental set-up (0.06 kg/s) before being set at 0.008 kg/s. Data are recorded once steady-state is obtained, i.e. once no significant change in measured data (pressure, temperature and mass flow rate) is observed.

Once steady state obtained, phase-change phenomena observed are recorded with a high-speed camera at a record rate of 250 frame per seconds and a resolution of 640 pixels by 920 pixels. Then these data are processed using a home-made Matlab program based on image intensity gradients in order to track bubbles flowing on the evaporator. This program works roughly as follows: after the image processing based on image intensity gradient is done, a morphological closing and a morphological erosion algorithms are used to close and reduce the size of the detected objects. These processes allow detecting the edges of the bubble with an accuracy of the order of a pixel (Fig. 3). Then, to prevent the detection of non-wanted objects, a circular condition is introduced: if C < 0.4 (Eq. 2), the object is rejected from the detection process. Another discriminating condition is used: objects in contact with the edge of the image are rejected as well. Objects thus detected are then tracked with a process based on Kalman filter so at the end of the process, information on location and size of each objects for each video is given.

$$C = \frac{4\pi A}{P^2} \qquad \text{Eq. (2)}$$

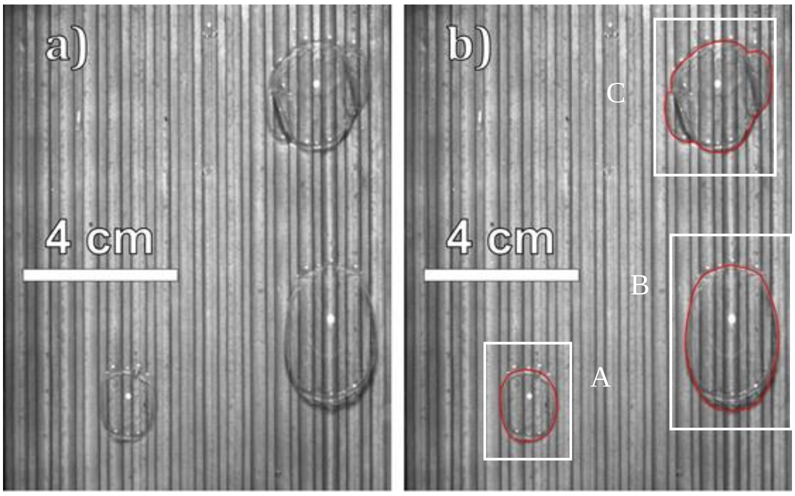

Figure 3: Example of object detected with the home-made Matlab program

3. BUBBLE FLOW ANALYSIS

3.1. Bubbles size discrimination

Several different phenomena in terms of bubbles size, bubbles velocity, bubbles behaviour, etc. are observed. As a first attempt to classify observed phenomena, bubbles are classified in three main categories: small size bubbles, medium size bubbles and large size bubbles. Small size bubbles are characterized by a bubble size smaller or of the same order of magnitude as the groove width (i.e. apparent diameter of 4 mm or smaller which leads to apparent area of 0.125 cm² or smaller). Medium size bubbles are defined by bubbles of two grooves width (plus the width of the fins), which correspond to apparent diameter ranging from 4 mm to 14 mm and apparent area ranging from 0.126 cm² to 1.539 cm² (bubble A in Fig. 3). Bubbles larger than 14 mm of apparent diameter (1.539 cm² of apparent area) are considered as large size bubbles (Bubble B in Fig. 3).

Based on these definitions, among 648 bubbles observed by naked eyes visualisation on arbitrary chosen videos, 94.3 % are classified as small size bubbles, 5.4 % on medium size bubbles and 0.3 % on large size bubbles. Automatic calculation of the area by the program led to, on these same videos, 1102 detected objects, 77.77 % of small size bubbles, 20.55 % of medium size bubble and 1.7 % of large size bubble. The overestimation of observed bubbles could be due to: (1) the detection of light reflection on grooves counted as object; (ii) the fact that a single bubble could be counted several times since the program may lose the bubble for several frames before detecting it again (if the bubble is lost for a longer period than 5 frames and then detected again, it is counted as two different objects). The larger proportion of medium size bubbles and large size bubbles can be due to, like observed in Fig. 3 – Bubbles C, (i) the possible detection of several bubbles through a same object, (ii) a slight overestimation of the area through the closing algorithm. Indeed, two main clusters of bubbles are observed: clusters of bubbles located on different location (on the fin, grooves, etc.) like in Fig. 4a) and clusters of bubbles located on the same grooves forming a train line (Fig. 4b).

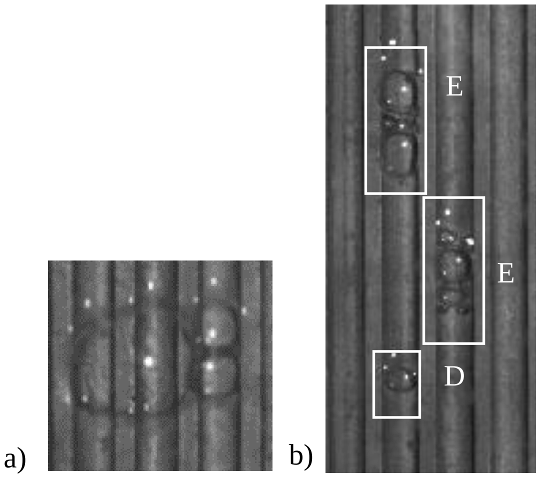

Figure 4: Example of clusters of bubble observed a) on several grooves; b) in the same groove forming a train line

These clusters are considered as a same object and the associated area is the area of the whole cluster. More generally, observed phenomena are the following:

- Single bubble of a channel size or smaller flowing inside a groove (Bubble D in Fig. 4);
- Bubbles train line flowing inside the groove. These bubbles can detach from each other to form two trains. Two train lines of bubbles can also, at a given time, form a single train line.
- Middle or large size bubbles flowing and eventually growing. While flowing, they can also gather with one another and form a cluster like shown in Fig. 4a.

It is worth noting that, according to phenomena observed on Fig.4, the working fluid (initially degassed water) might be polluted some way by water-glycol (secondary fluids). The working fluid thus might be water with a small amount of glycol. Although this assumption could be validated by naked eyes observation at the end of the experimental campaign (consistence of the fluid and smell), a precise estimation of glycol concentration was not conducted.

3.2. Probability density functions of experimental bubble flow velocities

Data obtained after the image processing are further processed with the help of a Savitzky-Golay filter on the location of the bubbles in order to calculate the flow velocity. This later is then simply calculated through a basic explicit scheme. A total of more than 10^8 data of each studied parameters (velocity and size) are obtained and processed. The probability density function of these data for the whole experimental domain is given in Fig. 5.

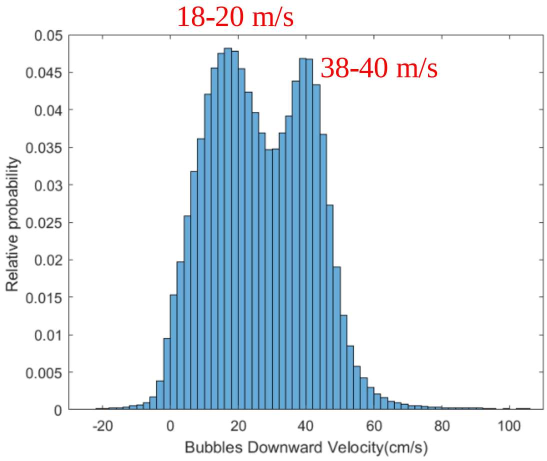

Figure 5: Probability density function of the velocity of the detected objects

For comparison purpose, Fig. 6 shows the velocity field inside a falling film for a mass flow rate of 0.008 kg/s (which correspond to Reynold number of around 200) assuming a Nusselt flow and a perfectly flat film (Collignon and Stutz, 2023). The highest calculated velocity in this field is 86.4 cm/s and the mean flow velocity is 53.7 cm/s

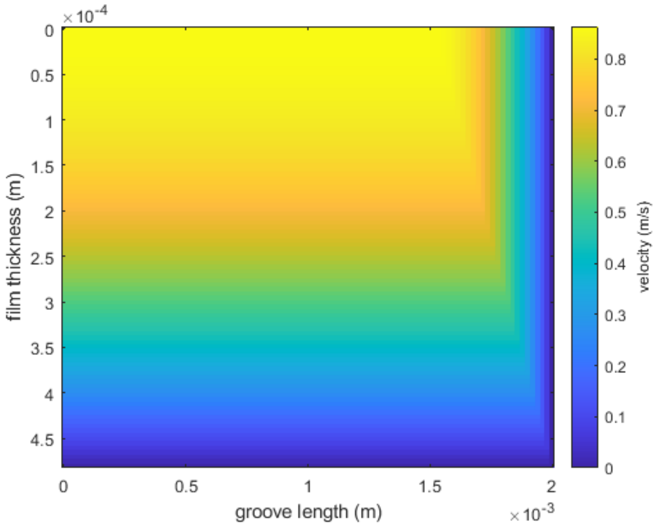

Figure 6: Velocity field inside the groove assuming a Nusselt flow and a perfectly flat film

The calculated bubbles velocity mainly ranges between - 2 cm/s and 80 cm/s (Fig. 5). Negatives velocities are due to the calculation process (explicit scheme on centroid position) and light reflections on grooves processed as a bubble.

A velocity up to 221 cm/s was estimated for some objects. These high velocities (ranging between 70 cm/s and 221 cm/s) are consequences of droplet, projected by bursting bubbles, in free fall between the evaporator and the camera.

For around 4,8 % of the data (one class of data in Fig. 6), the estimated velocity is in the range of 18-20 cm/s and 4,8 % are in the range of 38-40 cm/s. These velocities are slower than the mean velocity obtained in the case of a Nusselt flow for a perfectly plane film (53.7 cm/s). It is also lower than the velocity calculated by the formulation given by Bui and Dhir (1985) and obtain assuming a bubble subjected to drag and buoyancy forces (Eq. 3).

$$U_{bubble} = 0.37 \left[\frac{(\rho_l - \rho_v)g}{\rho_l {\nu_l}^{1/2}}\right]^{2/3} d \qquad \text{Eq. (3)}$$

According to Eq. 3, the calculated velocities for bubble of 4 mm of diameter to 14 mm of diameter range between 64 cm/s and 227 cm/s. In this calculation, viscous and form drag are assumed equal. However, due to the low vapor viscosity, viscous drag might be negligible compared with the form drag. In addition, if we consider the two following possibilities: (i) for small size bubbles, the bubbles are embedded deeply inside the falling film (Fig. 7a); (ii) for medium to large size bubbles, bubbles are in contact with the edges or the fins of the grooves (Fig. 7b); velocities observed should be different and surface tension should impact the bubble's behaviour. Indeed, in the latter case, the meniscus thus created imposed a given over-pressure inside the bubble. The curvature of the bubble is thus lower (Laplace's equation) and the form drag higher. On the other hand, since the over-pressure inside the bubble is lower in the case schematized in Fig. 7a, small-size bubbles should be more responsive to surface tension phenomena. In addition, for large size bubbles, there might be a contact with the double interface vapor-liquid- vapor of the bubble and the fins that constitute the grooves. In order to go deeper into the understanding of this observation and, as a first approach, the analysis of a single video leading to similar velocity probability density function is conducted.

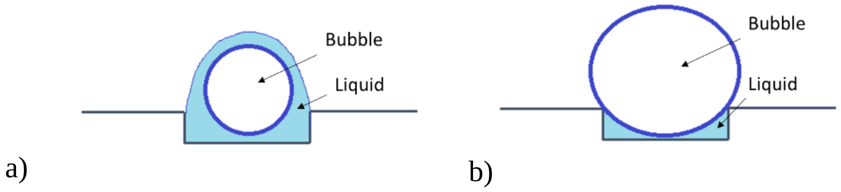

Figure 7: Schematic view of two possible bubbles' behaviour for a) small size bubbles b) medium size bubbles

3.3. Analysis of a single video T_{sat} = 12.5 °C, $\Delta T_{th,max}$ = 8 K

Similar trends as the one observed in Fig. 5 are obtained for experiments conducted at T_{sat} = 12.5 °C and $\Delta T_{th,max}$ = 8 K. Compared to Fig. 5, data were further processed in order to remove detected object that are not bubbles. As assumed for Fig. 5, this process indeed allows to remove the high probability density function ranging between -2 cm/s and 2 cm/s. In this Fig. 7, for around 10.5 % and 5.2 % of the data, the estimated velocity respectively ranges between 8 cm/s -10 cm/s and 44 cm/s-46 cm/s. For this same video 6.6 % of bubbles are detected as large size bubbles, 47.2 % as medium size bubbles and 46 % as small size bubbles. Fig. 8 shows the apparent bubble area versus the estimated velocity.

For this video, large bubbles have relatively low velocities. The mean velocity of the three bubbles detected as large bubbles ranges between 8 cm/s and 16 cm/s. One of these three large bubbles, represented by blue crosses in Fig. 8, is the cluster of bubbles shown in Fig. 4a. The bubble showing the similar behaviour is a bubble similar to the bubble A in Fig. 3. Green crosses represent the velocities of a bubbles train constituted of two small size bubbles. The cluster of bubbles (Fig. 4a) and the large bubble thus behave similarly and their velocities are relatively constant, in the range of 8 cm/s and 10 cm/s. The surface tension probably makes it possible to maintain the two bubbles in a single integral and non-deformable object.

Small and medium size bubbles flow at different velocities. Two different behaviours are observed. Fig. 9 shows the time-evolution (in number of frames) of the velocity for 8 bubbles: 4 of them with relatively low velocities (mean velocity close to 10 cm/s - Fig. 9a) and 4 others with relatively high velocities (mean velocity close to 44 cm/s - Fig. 9a). For relatively low velocity (Fig. 9a), the bubble velocity seems to decrease and then, for some bubbles increase again. For relatively high velocity (Fig. 9b), the bubble velocity increases until it reaches a plateau. These observations are to be linked with the location of the bubble and the time at which it was detected. Indeed, bubbles observed in Fig. 9a were detected on the right side of the evaporator, at the time it reaches the middle height of the evaporator. On the other hand, bubbles on Fig. 9b are bubbles observed at the middle width of the evaporator and at the top of this one. The observed increase of velocity in Fig. 9b is thus due to the bubble detachment from the distributor and to the time required to reach an established speed. It is worth noting also that at the top right of the evaporator, large bubbles collapsing before detachment are observed. These bubbles might prevent an efficient feeding of the groove leading to a non-homogeneous distribution of the flow. The mass flow rate at the right side of the evaporator must be much smaller than the one at the middle width of the evaporator.

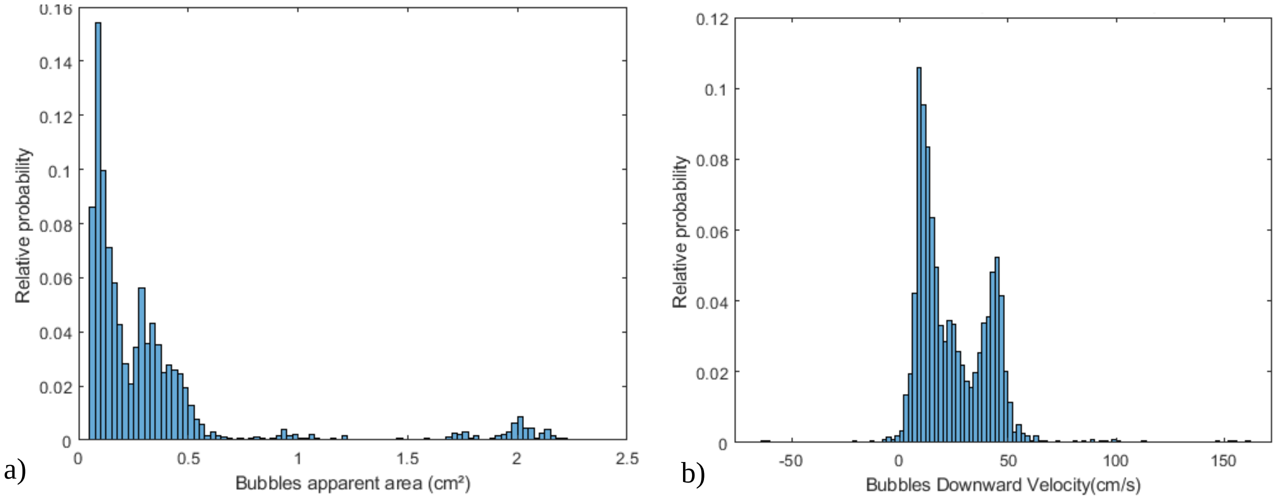

Figure 7: Probability density function on a) the area, b) the velocity of detected objects (T_{sat} = 12.5 °C and $\Delta T_{th,max}$ = 8K)

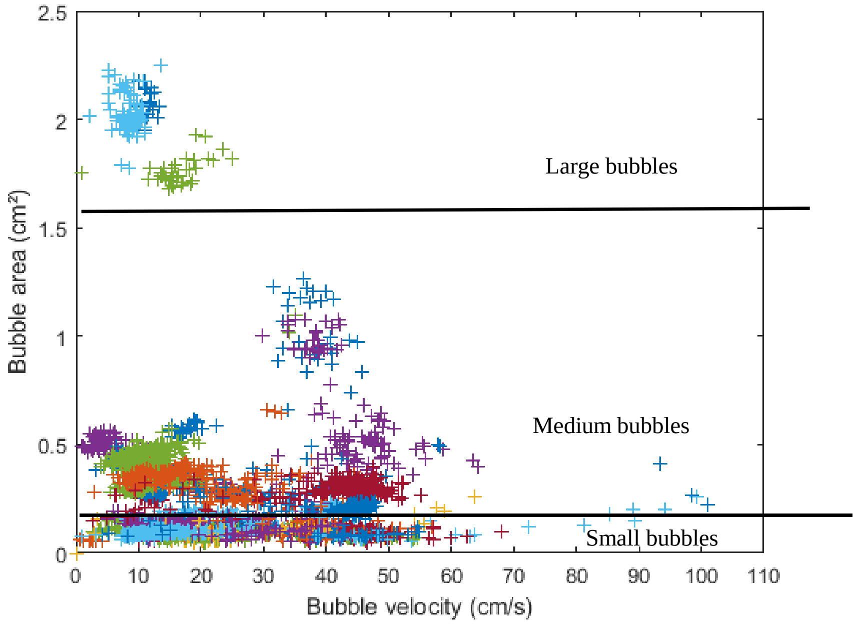

Figure 8: Map of the instantaneous bubbles' velocity with its apparent area (T_{sat} = 12.5 °C and $\Delta T_{th,max}$ = 8K). Each colour represents a different bubble.

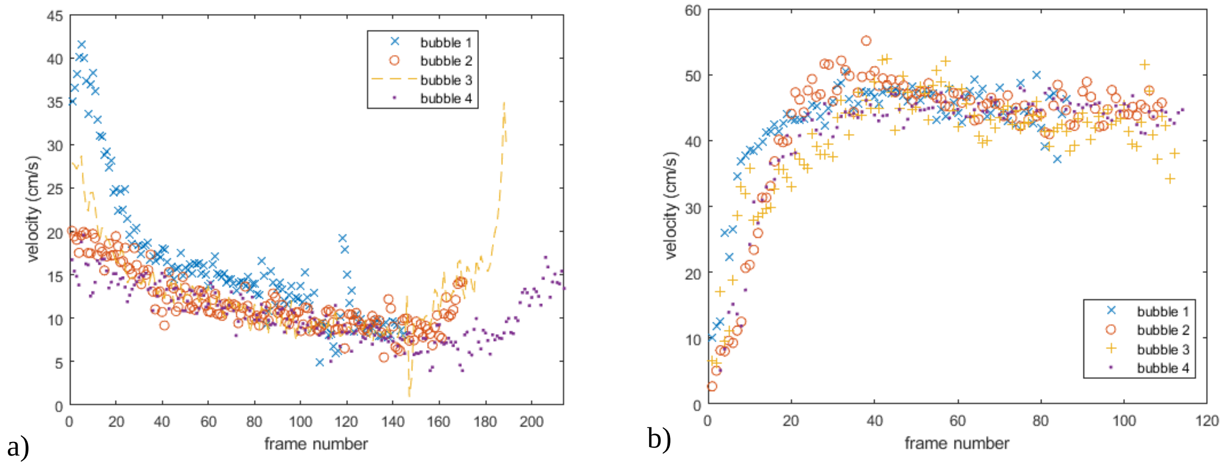

Figure 9: Time evolution (in number of frames – time step 4 ms) of the velocity for chosen small to medium bubbles a) for a mean velocity close to 10 cm/s, b) for a mean velocity close to 44 cm/s (T_{sat} = 12.5 °C and $\Delta T_{th,max}$ = 8K)

4. CONCLUSIONS

This paper introduces preliminary results obtained during the study of water falling film boiling in the context of falling film evaporator. Conditions set are representatives to those obtained in the evaporator of a water chiller. Working pressures from 1 to 2.4 kPa are investigated. Maximal theoretical wall superheat from 1 K to 10 K are set. Phase-change phenomena observed are recorded with a high-speed camera and data obtained processed with a home-made program to obtain the bubbles size and velocity. Two mains populations are observed. Bubbles with a travel speed ranging between 18 cm/s – 20 cm/s, and bubbles with a travel speed ranging from 38 cm/s – 40 cm/s. A deeper analysis of a single video (T_{sat} = 12.5 °C and $\Delta \boldsymbol{T_{th,max}}$ = 8K) leads to similar result with two mains behaviours: bubbles with a mean flow velocity of around 10 cm/s and bubbles with a mean flow velocity of around 44 cm/s. It is shown that, for this video, a large bubble or a cluster of bubbles behave almost similarly with a relatively slow velocity. Cluster of bubbles thus behave like a large bubble, being probably subject to higher form drag and higher buoyancy forces compared with small size bubbles. For small and medium sizes bubbles, it is shown that the estimated velocity depends on the localisation of the bubbles: bubbles observed on the right side of the evaporator have slower velocities than bubbles located at the middle width of the evaporator. This observation is probably due to the occurrence of boiling and collapsing of bubbles at the outlet of the distributor on this right side. The mass flow rate is thus probably highly reduced at this localisation. In future works, the analysis conducted for the single video will be generalized to the 199 videos processed. The main trends will be highlighted and modelized through simple models. In particular, the form drag force around the bubble will be estimated. The impact of the boiling events and the flow of bubbles on the evaporator performance will be quantified.

NOMENCLATURE

A	Area (m²)	T_{sat}	Saturation temperature (K)
d	Diameter (m)	T_{cd}	Temperature of the secondary fluid at the condenser (K)
g	Gravitational acceleration ($m.s^{-2}$)	$\Delta T_{th,max}$	Temperature difference (K)
P_{sat}	Saturation pressure (Pa)	U	Velocity (m/s)
P_{tank}	Vacuum vessel pressure (Pa)	ρ	Density (kg/m3)
P	Perimeter (m)	ν_l	Kinematic Viscosity (m²/s)

REFERENCES

Bock, B. D., Meyer, J. P., & Thome, J. R. (2019). Falling film boiling and pool boiling on plain circular tubes: Influence of surface roughness, surface material and saturation temperature on heat transfer and dryout. *Experimental Thermal and Fluid Science*, *109*, 109870.

Bui T. D., Dhir V. K. (1985). Film Boiling Heat Transfer on an Isothermal Vertical Surface.

Cerza, M., & Sernas, V. (1985). A bubble growth model for nucleate boiling in thin, falling, superheated, laminar, water films. *International journal of heat and mass transfer*, *28*(7), 1307-1316.

Collignon, R., & Stutz, B. (2023). Numerical simulation and modeling of the heat and mass transfer in a grooved flat falling film evaporator. *International Journal of Refrigeration*.

Giraud, F., Rullière, R., Toublanc, C., Clausse, M., & Bonjour, J. (2015). Experimental evidence of a new regime for boiling of water at subatmospheric pressure. Experimental thermal and fluid science, 60, 45-53.